Nanoscale

Discrimination of Adhesion and Viscoelasticity from Nanoscale Maps of Polymer Surfaces using Bimodal Atomic Force Microscopy

Journal:	*Nanoscale*
Manuscript ID	NR-ART-05-2021-003437.R1
Article Type:	Paper
Date Submitted by the Author:	29-Aug-2021
Complete List of Authors:	Rajabifar, Bahram; Purdue University, Mechanical Engineering Bajaj, Anil; Purdue University, School of Mechanical Engineering Reifenberger, Ronald; Purdue University, Department of Physics Proksch, Roger; Asylum Research, Raman, Arvind; Purdue University, School of Mechanical Engineering and the Birck Nanotechnology Center

Discrimination of Adhesion and Viscoelasticity from Nanoscale Maps of Polymer Surfaces using Bimodal Atomic Force Microscopy

Bahram Rajabifar [1,2], Anil Bajaj [1], Ronald Reifenberger [2], Roger Proksch [3], Arvind Raman [* 1,2].

1. School of Mechanical Engineering, Purdue University, 585 Purdue Mall, West Lafayette, IN 47907, United States

2. Birck Nanotechnology Center, 1205 W State Street, West Lafayette, IN 47907, United States

3. Asylum Research, an Oxford Instruments company, Santa Barbara, CA, 93117, USA

Abstract

The simultaneous excitation and measurement of two eigenmodes in bimodal atomic force microscopy (AFM) during sub-micron scale surface imaging augments the number of observables at each pixel of the image compared to the normal tapping mode. However, a comprehensive connection between the bimodal AFM observables and the surface adhesive and viscoelastic properties of polymer samples remains elusive. To address this gap, we first propose an algorithm that systematically accommodates surface forces and linearly viscoelastic three-dimensional deformation computed via Attard's model into the bimodal AFM framework. The proposed algorithm simultaneously satisfies the amplitude reduction formulas for both resonant eigenmodes and enables the rigorous prediction and interpretation of bimodal AFM observables with a first-principles approach. We used the proposed algorithm to predict the dependence of bimodal AFM observables on local adhesion and standard linear solid (SLS) constitutive parameters as well as operating conditions. Secondly, we present an inverse method to quantitatively predict the local adhesion and SLS viscoelastic parameters from bimodal AFM data acquired on a heterogeneous sample. We demonstrate the method experimentally using bimodal AFM on polystyrene-low density polyethylene (PS-LDPE) polymer blend. This inverse method enables the quantitative discrimination of adhesion and viscoelastic properties from bimodal AFM maps of such samples and opens the door for advanced computational interaction models to be used to quantify local nanomechanical properties of adhesive, viscoelastic materials using bimodal AFM.

* Corresponding Author. E-mail: raman@purdue.edu

1. Introduction

The continuing need for sub-micron scale compositional imaging of complex material surfaces has led to the increased use of multi-frequency AFM methods. Bimodal AFM is a popular subset of multi-frequency AFM methods[1] that provides additional information channels beyond the traditional Amplitude-Modulated AFM (AM-AFM) or tapping mode. AM-AFM usually requires a trade-off between greater compositional contrast and greater imaging forces which may be detrimental for the fragile samples.[2] Bimodal AFM can enhance achieved compositional contrast while applying gentle imaging forces without damaging the surface.[3-8] In bimodal AFM the microcantilever is excited at its fundamental eigenmode frequency along with an additional small amplitude "perturbation" excitation of a higher flexural eigenmode (secondary eigenmode) (Figure 1)[1, 9]. The resulting tip motion occurs at different timescales, a slow timescale corresponding to that of the fundamental mode and a fast timescale corresponding to the higher excited eigenmode. The lock-in amplifiers demodulate and measure the averaged amplitude and phase of tip motion at the two excitation frequencies.

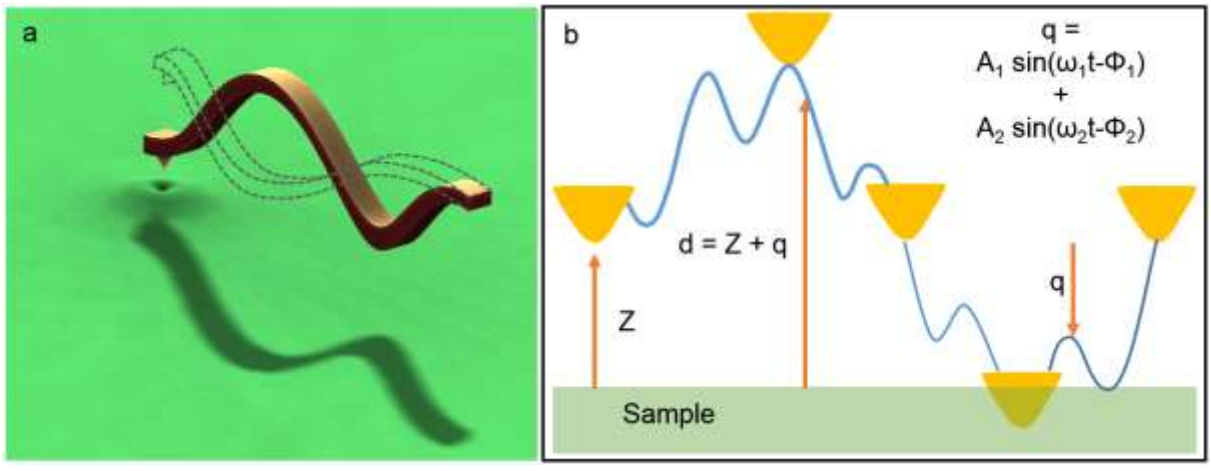

Figure 1. (a) Bimodal AFM simultaneously excites the first and a higher eigenmode of the microcantilever. (b) The resulting tip trajectory is assumed to be the sum of two harmonics whose steady-state amplitudes and phases change due to the tip-sample interaction and the microcantilever properties. In this figure, ω_i is the excitation frequency and A_i and ϕ_i are the amplitude and phase lag relative to the excitation force of the i^{th} mode, respectively. Z and $d(t)$ are the distance of the microcantilever base and tip with respect to the undeformed surface level, respectively. $q(t)$ is the microcantilever tip deflection.

Bimodal AFM scans of a surface are characterized by three observables at each pixel in addition to the topography, regardless of the feedback control loops used. There are many ways to configure the feedback control loops to operate bimodal AFM [7, 10, 11]. In the most direct and commonly used configuration, the amplitude of the first mode is similarly regulated at a fixed setpoint amplitude by adjusting the Z distance and the slow-timescale averaged phase of the fundamental mode and the amplitude and phase of the secondary mode are allowed to respond to changes in local surface properties (AM-AM)[12]. In the other common feedback loop arrangement, AM-FM, the first mode's amplitude is regulated by adjusting the Z distance. However, the secondary mode's averaged phase lag is held fixed by changing the excitation frequency through a Phase Locked Loop (PLL) and its amplitude is maintained constant by adjusting the excitation magnitude. Here the secondary mode's excitation amplitude provides a measure of the tip-sample dissipation. During imaging, the slow-timescale averaged phase lag of the fundamental mode and frequency shift and dissipation of the secondary mode at each pixel are recorded. Finally, in FM-FM, two PLLs and drive modulation are used to regulate the slow-timescale averaged amplitudes and phases of both modes [10]. The three observables for these most common implementations of bimodal AFM: AM-AM, AM-FM, and FM-FM are listed in Table 1[13]. The required feedback loops for these bimodal AFM configurations are different and the associated control schemes become more complicated in the order listed in Table 1.

Table 1. Three observables of the most common modalities of bimodal AFM.

	Observable #	1	2	3
	Mode #	First mode	Secondary mode	Secondary mode
Config. 1	AM-AM	Phase (ϕ_1)	Phase (ϕ_2)	Amplitude (A_2)
Config. 2	AM-FM	Phase (ϕ_1)	Freq. shift (Δf_1)	Drive (D_2)
Config. 3	FM-FM	Freq. shift (Δf_1)	Freq. shift (Δf_1)	Drive (D_2)

Quantitative bimodal AFM on polymeric surfaces requires the pixel-by-pixel inversion of three observables of the mode to extract quantitative maps of local polymer properties. Garcia et al. used an energy balance theory method to link the bimodal AM-FM

observables to the material viscoelastic properties.[14, 15] The method is based on a simple Hertzian contact model for tip-sample interaction force with *ad hoc* addition of a Kelvin-Voigt viscoelastic element without any surface forces (adhesion). In another work[7], the *ad hoc* tip-sample viscoelastic model approach[14] was extended to a fractional calculus-based method to calculate the material viscoelastic properties. Proksch et al.[16] used the Oliver and Pharr method[17] to link the tip-sample interaction stiffness to the contact radius. They calculated the tip-sample interaction using a Hertz model's elastic generalization and neglect the velocity-dependency of the tip-sample interaction force and long-range surface forces. All these prior-tip sample interaction models have the advantage that when combined with energy balance laws for each mode, they offer simple closed-form expressions that allow the inversion of bimodal AFM observables to quantitative estimates of the local elastic/viscoelastic properties.

However, one of the major shortcomings of these prior inversion approaches is that they utilize simple or *ad hoc* tip-sample models which are limited in their ability to represent tip contact with soft, adhesive, and viscoelastic surfaces. Specifically: (a) *ad hoc* viscoelastic models are unable to accurately predict the tip-detachment from the surface[7, 18, 19] and are unable to predict surface relaxation post-detachment (b) they can lead to artifacts such as the presence of apparently attractive forces[20] even if the model does not contain attractive forces, and (c) they do not include attractive/adhesive forces. These shortcomings can lead to artifacts in estimated parameters, especially on soft viscoelastic adhesive samples. In one example, a bimodal AFM map inversion based on an *ad hoc* viscoelastic model[7] led to an effective viscosity prediction for PS domain in a PS-LDPE blend to be 4 times greater than the viscosity for the LDPE domain when measured in the same scan. This ratio of predicted damping characteristics[7] for stiff PS, which is glassy at room temperature, and soft LDPE which is rubbery at room temperature is not physically acceptable.

Among all the available continuum mechanics-based tip-sample interaction models for polymer samples, Attard's model[21, 22] is arguably the most accurate model to capture the physics of the interaction between a rigid axisymmetric tip and a polymer surface. The model accounts for finite range surface forces as well as the sample's full three-

dimensional viscoelasticity with arbitrary constitutive linear viscoelastic relations. Attard's computational approach, which is based on the Boussinesq solution for a semi-infinite half-space [23] and introduces temporal and radial discretization, uses a completely different methodology when compared to the classical contact models. Attard's model has significant advantages relative to models that use an *ad hoc* approach to add viscoelasticity to DMT or Hertz based models:

1. Hertz- and DMT-based models with *ad hoc* Kelvin-Voigt elements assume a certain dependence of contact area on indentation depth regardless of history of deformation. The history dependence of the contact area was studied by Ting[24] but his approach does not include surface forces. Attard's model inherently addresses this dependence since it solves a 3-dimensional linear viscoelastic deformation problem without assumptions on contact area evolution. As a result, the detachment of the tip from the surface is correctly computed, unlike in the *ad hoc* viscoelastic models.
2. Hertz and DMT approaches with *ad hoc* Kelvin Voigt viscoelasticity are generally unable to predict viscoelastic dissipation when the tip oscillates in the attractive regime. Since Attard's model includes surface forces it allows for the viscoelastic surface to deform and relax and dissipate energy even if the tip oscillates in attractive regime with the surface.
3. A viscoelastic surface will continue to relax as the oscillating tip detaches and moves away from the surface. This is an expected surface behavior that is not predicted by *ad hoc* Kelvin Voigt elements added on to classical contact mechanics models.
4. Finally as shown elsewhere[20] *ad hoc* Kelvin Voigt modifications of classical contact mechanics models can lead to artifacts such as the creation of negative tip-sample interaction forces even in the absence of surface forces. Attard's model systematically includes both general surface force models as well as linear 3-dimensional viscoelasticity of the sample surface and avoids these artifacts.

Converting bimodal observables to quantitative properties based on the Hertz/DMT models with *ad hoc* Kelvin Voigt viscoelasticity may provide less inaccurate results on stiff

samples with low adhesion and low viscoelasticity. However, to establish a relationship between bimodal AFM observables and local physical properties of soft, adhesive, and highly viscoelastic materials it may be desirable to use more accurate models such as Attard's model.

However, Attard's model is computationally expensive due to the presence of iterative loops and spatial (radial) and temporal discretization. Moreover, Attard's computational approach requires a priori knowledge of the tip trajectory relative to the surface as an input to compute the history of surface deformation and interaction forces during the contact time. Thus, its implementation in all dynamic AFM methods is not directly possible since the resonant probe's amplitude and phase at a given distance of the unperturbed cantilever from the sample are in fact the output of the tip-sample interaction and the cantilever dynamics. For both these reasons, it has been challenging to use Attard's model to make predictions for dynamic AFM modes.

In this work, we develop an algorithm including Attard's model to link the surface properties of an adhesive and viscoelastic sample to associated AM-AM bimodal AFM observables. The algorithm has several advantages: (1) it can easily be adapted to other implementations of bimodal AFM such as AM-FM or FM-FM bimodal operation, (2) it simultaneously satisfies the amplitude reduction formulas for both excited modes in AM-AM bimodal AFM, and (3) it requires the computation of tip-surface interaction and surface deformation history which is implemented here using an accelerated computational approach[20] for Attard's model which is more than two orders of magnitude faster than the original implementation[21, 22].

We use the proposed algorithm to illustrate the dependence of the bimodal AFM observables on the properties of adhesive, viscoelastic surfaces modeled by Lennard Jones pressure and SLS viscoelastic constitutive relations. Then, we present an approach to invert the three bimodal AFM parameters using a linear regressive model based on the forward computations carried out over a vast range of sample parameters selected by the Latin hypercube sampling method[25]. The computational regressive model, applicable for the specific cantilever and operating conditions, then relates physical properties of the local polymer such as adhesion, long- and short-term elastic

moduli, to the three AM-AM bimodal AFM observables via a computed 3 by 3 matrix. The three observables measured at each pixel can then be converted to quantitative estimates of these physical properties via matrix inversion at each pixel and that relates the observables to physical polymer properties. Thus, this approach can quantitatively discriminate between adhesion and viscoelastic properties which is normally considered very challenging for adhesive viscoelastic samples. The approach is demonstrated using experimental measurements using AC160 cantilevers on a PS-LDPE sample. The resulting quantitative maps of adhesion, long- and short-term elastic moduli are in line with ones reported in literature [14, 26, 27].

2. Theory

We model the transverse vibrations of the microcantilever, $w(x,t)$, with Euler-Bernoulli partial differential equation (PDE) for a beam with a rectangular cross-section, as follows:

$$\rho_c A_c \ddot{w}(x,t) + F_{hydro}\left(\dot{w}(x,t), \ddot{w}(x,t)\right) + E_c I_c w''''(x,t) = F_{ts}(d,\dot{d})\,\delta(x - L_c) + F_{direct}(x,t), \qquad (1)$$

where, x, t, ρ_c, A_c, E_c, I_c, and L_c are the longitudinal distance from the base of the microcantilever, time, the linear density, cross-sectional area, elastic modulus, area moment, and tip location distance from the base of the microcantilever, respectively. $\dot{w}(x,t)$ and $\ddot{w}(x,t)$ are the first and second derivatives of $w(x,t)$ respect to t, respectively and $w''''(x,t)$ is the fourth derivative of $w(x,t)$ with respect to x. d and $\dot{d}$ are the tip-sample gap and its velocity relative to the undeformed surface level as shown in Figure 1. $F_{hydro}(\dot{w}(x,t), \ddot{w}(x,t)) = \bar{F}_{hydro}(x,t)$ is the uniformly distributed hydrodynamic force per unit length computable in the frequency domain using Sader's method [28], acting on the oscillating microcantilever. The tip-surface interaction force, $F_{ts}(d,\dot{d})$, which acts locally at the tip location is described with a Dirac delta function, δ. The direct microcantilever excitation [29], i.e. via photothermal, magnetic, or Lorentz for excitation, exerts a spatio-temporal distributed force per unit length, $F_{direct}(x,t)$. Dither piezo excitation will be included through the boundary conditions as described later in this section. The absolute deflection of the microcantilever is composed of the Z-piezo motion, $Z(t)$, the dither-piezo

motion, $y(t)$, and the transverse vibration in the non-inertial frame attached to the base, $u(x,t)$:

$$w(x,t) = Z(t) + y(t) + u(x,t). \tag{2}$$

Substituting Eqn. (2) in the beam PDE, Eqn. (1), the equation of motion can be cast into the moving reference frame attached to the base of the microcantilever:

$$\rho_c A_c \ddot{u}(x,t) + F_{hydro}\left(\ddot{y}(t) + \ddot{u}(x,t) + \ddot{Z}(t), \dot{y}(t) + \dot{u}(x,t) + \dot{Z}(t)\right) + E_c I_c u''''(x,t) = F_{ts}(d,\dot{d})\,\delta(x - L_c) + F_{direct}(x,t) - \rho_c A_c\left(\ddot{y}(t) + \ddot{Z}(t)\right), \tag{3}$$

and the corresponding boundary conditions, ignoring the tip-mass effect become:

$$u(0,t) = 0, \qquad u'(0,t) = 0, \qquad u''(L_c,t) = 0, \qquad u'''(L_c,t) = 0. \tag{4}$$

For bimodal operation, excitation forces are applied at two eigenfrequencies of the microcantilever, $i = 1$, or fundamental mode frequency, and $i = 2$ or secondary mode frequency. The secondary mode is often the second eigenmode of the microcantilever, but it can instead be any higher-order eigenmode. As a result, we can combine the net external excitation on the microcantilever as the sum of direct excitation and inertial excitation:

$$\sum_{i=1}^{2} F_{drive,i}(x,t) = F_{direct}(x,t) - \rho_c A_c \ddot{y}(t), \tag{5}$$

where $F_{drive,i}(x,t)$ are the net forcing functions at the two different drive frequencies. Therefore, we discretize Eqn. (3) using Galerkin's method to project the dynamics onto the microcantilever's eigenmodes:

$$u(x,t) = \sum_{i=1}^{2} \bar{\Phi}_i(x)\, q_i(t), \tag{6}$$

where $\bar{\Phi}_i(x)$ and $q_i(t)$ describe the microcantilever eigenmodes of free vibration and the associated generalized coordinates, respectively. The mode shapes are normalized so

that $\bar{\Phi}_i(L_c) = 1$ for each of the eigenmodes[30] and the generalized coordinates represent the tip motion in each eigenmode:

$$\rho_c A_c \sum_{i=1}^{2} \bar{\Phi}_i(x)\, \ddot{q}_i(t) + F_{hydro}\left(\sum_{i=1}^{2} \bar{\Phi}_i(x)\, \ddot{q}_i(t), \sum_{i=1}^{2} \bar{\Phi}_i(x)\, \dot{q}_i(t) \right) + E_c I_c \sum_{i=1}^{2} \bar{\Phi}_i''''(x)\, q_i(t) = F_{ts}(d,\dot{d})\, \delta(x - L_c) + \sum_{i=1}^{2} F_{drive,i}(x,t)\,. \tag{7}$$

Next, we use the biorthogonality of $\bar{\Phi}_i(x)$ terms to extract the discretized equations of motion of excited modes by multiplying Eqn. (7) once with $\bar{\Phi}_1(x)$ and then with $\bar{\Phi}_2(x)$, and then integrating respect to x. The resultant ODEs are:

$$\left(\rho_c A_c \int_0^{L_c} \bar{\Phi}_i^{\,2}(x)dx \right) \ddot{q}_i(t) + \int_0^{L_c} F_{hydro}\left(\sum_{i=1}^{2} \bar{\Phi}_i(x)\, \ddot{q}_i(t), \sum_{i=1}^{2} \bar{\Phi}_i(x)\, \dot{q}_i(t) \right) \bar{\Phi}_i(x)dx + \left(E_c I_c \int_0^{L_c} \left(\bar{\Phi}_i''(x) \right)^2 dx \right) q_i(t) = F_{ts}(d,\dot{d}) + \int_0^{L_c} \bar{\Phi}_i(x) \sum_{i=1}^{2} F_{drive,i}(x,t)\, dx\,. \tag{8}$$

In order to simplify the F_{hydro} term, we note that in bimodal AFM operation the cantilever response generally combines harmonic motion at two discrete frequencies. Under these conditions it is reasonable to approximate the Fourier transform of F_{hydro} [28] as follows:

$$\bar{F}_{hydro}\left(x|\omega\right) = \int_{t=-\infty}^{\infty} \bar{F}_{hydro}\left(x,t\right) e^{-j\omega t} dt = \frac{\pi}{4} \rho\, \omega^2\, b_c^{\,2}\, \Gamma(\omega) \sum_{i=1}^{2} \bar{\Phi}_i(x) \int_{t=-\infty}^{\infty} q_i(t)\, e^{-j\omega t} dt\,, \tag{9}$$

where, ρ, b_c, and $\Gamma(\omega)$ are the air mass density, nominal width of the microcantilever, and the dimensionless complex-valued hydrodynamic function, respectively and $j^2 = -1$. Γ includes an imaginary and a real dimensionless component, Γ_i and Γ_r, respectively[31]. The hydrodynamic force per unit length on the microcantilever can be converted into two frequency-dependent parameters: effective modal damping, $\hat{c}(\omega)$, and added mass, $\hat{M}(\omega)$ [28]. However, since the excitation forces in bimodal operation are applied on relatively narrow frequency ranges, the frequency dependence of $\hat{c}(\omega)$ and $\hat{M}(\omega)$ is weak and we can safely express them as follows:

$$m_i^* = \hat{M}(\omega_i),$$
$$c_i^* = \hat{c}(\omega_i), \tag{10}$$

where $\omega_i, (i = 1, 2)$ are the air mass-loaded natural frequencies of the two modes defined as [32]:

$$\omega_i^2 = \frac{\left(E_c I_c \int_0^{L_c} \left(\bar{\Phi}_i''(x) \right)^2 dx \right) \Big/ \left(\rho_c A_c \int_0^{L_c} \bar{\Phi}_i^2(x) dx \right)}{1 + (\pi/4)(\rho_c b_c / \rho h_c)\Gamma_r(\omega_i)}, \tag{11}$$

where, h_c is the nominal thickness of the microcantilever. Since employed $F_{drive,i}(x,t)$ for excited modes are harmonic, we write it down as a multiplication of a forcing magnitude and a harmonic term:

$$F_{drive,i}(x,t) = \tilde{F}_{drive,i}(x) \times \cos(\hat{\omega}_i t). \tag{12}$$

Combining Eqn. (8) and (12) and rearranging to include experimentally observable parameters, the beam's PDE reduces into two coupled ODEs as follows:

$$\begin{aligned} \frac{1}{\omega_1^2}\ddot{q}_1(t) + \frac{1}{\omega_1 Q_1}\dot{q}_1(t) + q_1(t) &= \frac{1}{k_1}F_{ts}(d,\dot{d}) + \frac{1}{k_1}F_{11}\cos(\hat{\omega}_1 t) + \frac{1}{k_1}F_{12}\cos(\hat{\omega}_2 t), \\ \frac{1}{\omega_2^2}\ddot{q}_2(t) + \frac{1}{\omega_2 Q_2}\dot{q}_2(t) + q_2(t) &= \frac{1}{k_2}F_{ts}(d,\dot{d}) + \frac{1}{k_2}F_{21}\cos(\hat{\omega}_1 t) + \frac{1}{k_2}F_{22}\cos(\hat{\omega}_2 t), \end{aligned} \tag{13}$$

where,

$$F_{kl} = \int_0^{L_c} \bar{\Phi}_l(x)\, \tilde{F}_{drive,i}(x)\, dx \quad , \; k, l = 1, 2, \tag{14}$$

and k_i, $\omega_i = 2\pi f_i$, and Q_i are equivalent stiffness, natural frequencies (rad/s), and quality factor of the i^{th} mode $(i = 1, 2)$, respectively. In this article, we will focus on the case where $\hat{\omega}_i = \omega_i$. Solutions of Eqn. (13) show that the effect of F_{kl} on tip motion when $i \neq j$ is negligible and can be ignored. Then, we express the discretized ODEs by re-writing the

excitation magnitudes in terms of the oscillation amplitudes in absence of the tip-sample interaction:

$$\begin{aligned}\frac{1}{\omega_i^2}\ddot{q}_1(t)+\frac{1}{\omega_i Q_i}\dot{q}_1(t)+q_1(t)&=\frac{1}{k_1}F_{ts}(d,\dot{d})+\frac{A_{01}}{Q_1}\cos(\omega_1 t),\\ \frac{1}{\omega_2^2}\ddot{q}_2(t)+\frac{1}{\omega_2 Q_2}\dot{q}_2(t)+q_2(t)&=\frac{1}{k_2}F_{ts}(d,\dot{d})+\frac{A_{02}}{Q_2}\cos(\omega_2 t),\end{aligned} \tag{15}$$

where, $d(t)=Z+q_1(t)+q_2(t)$, and A_{0i} is the "free" oscillation amplitude of the i^{th} mode, which is the forced steady-state amplitude in the absence of tip-sample interaction. Eqn. (15) represents the tip dynamics in bimodal AFM when the excitation frequencies exactly coincide with the natural frequencies. The method needs to be adapted if there is any intentional detuning between excitation and natural frequencies.

To derive amplitude reduction equations for bimodal AFM, we assume that the tip motion can be expressed as the sum of two harmonics at two different excitation frequencies, i.e.:

$$q(t)=q_1(t)+q_2(t)=A_1\cos(\omega_1 t-\phi_1)+A_2\cos(\omega_2 t-\phi_2), \tag{16}$$

where A_i and ϕ_i are the steady-state tip oscillation amplitude and phase lag of the i^{th} mode relative to its corresponding modal excitation force[13, 33]. This assumes that any slow time-scale amplitude and phase modulation leading to sidebands around the excited modes are considered negligible for amplitude reduction. It is also assumed that higher harmonics of the excited modes play a negligible role in the amplitude reduction at the two excitation frequencies, a condition generally met for air or in vacuum applications when higher eigenfrequencies are not integer multiples of the excited modes [34-36].

Next, we substitute $q_1(t)$ and $q_2(t)$ from Eqn. (16) into Eqn. (15):

$$\begin{aligned}-\frac{k_1}{Q_1}\left(A_1\sin(\omega_1 t-\phi_1)+A_{01}\cos(\omega_1 t)\right)&=F_{ts}(d,\dot{d}),\\ -\frac{k_2}{Q_2}\left(A_2\sin(\omega_2 t-\phi_2)+A_{02}\cos(\omega_2 t)\right)&=F_{ts}(d,\dot{d}).\end{aligned} \tag{17}$$

Then, we multiply Eqn. (17) with $q_i(t)$ and integrate with respect to time over 0 to $n_c T_1$. The coefficient n_c represents the number of slow time-scale periods that the mode parameters are computed and averaged over. This yields:

$$\begin{aligned} V_{ts,i} &= \frac{1}{n_c T_i}\int_0^{n_c T_i} F_{ts}\left(d,\dot{d}\right) q_i(t)dt = \frac{1}{n_c T_1}\int_0^{n_c T_1} F_{ts}\left(d,\dot{d}\right) A_i \cos(\omega_i t-\phi_i)dt = \\ &\qquad -\frac{k_i A_{0i} A_i}{2Q_i}\cos(\phi_i), \\ E_{ts,i} &= -\frac{1}{n_c}\int_0^{n_c T_i} F_{ts}\left(d,\dot{d}\right)\dot{q}_i(t)dt = \frac{T_i}{n_c T_1}\int_0^{n_c T_1} F_{ts}\left(d,\dot{d}\right)\times A_i\omega_i \sin(\omega_i t-\phi_i)dt = \\ &\qquad \frac{\pi k_i A_i A_{0i}}{Q_i}\left(\sin(\phi_i)-\frac{A_i}{A_{0i}}\right). \end{aligned} \tag{18}$$

Here, T_i, $V_{ts,i}$, and $E_{ts,i}$ are the time period, the average value of the virial (conservative interactions), and dissipation (non-conservative interactions) associated with the i^{th} mode during each interaction cycle[37]. $V_{ts,i}$ and $E_{ts,i}$ are computed and averaged over many time-periods of the fundamental mode ($n_c T_1$). This mimics the experimental conditions where lock-in amplifiers average these quantities for the two excited modes over the slow timescale. If the ratio of excitation frequencies is equal to the ratio of two integer numbers, the resultant bimodal tip trajectory is periodic, and it simplifies the parameters' calculation. However, the driving frequencies of the microcantilevers are generally incommensurate[38] and the tip motion can be quasi-periodic[39].

The amplitude reduction and phase lag formulas for the first and secondary modes are then attained by eliminating ϕ_i in Eqn. (18):

$$A_i^{ratio} = \frac{A_i}{A_{0i}} = \frac{\pi k_i A_i^2/Q_i}{\sqrt{\left(-2\pi V_{ts,i}\right)^2+\left(\frac{\pi k_i A_i^2}{Q_i}+E_{ts,i}\right)^2}}, \tag{19}$$

$$\phi_i = \tan^{-1}\frac{\pi k_i A_i^{\,2}/Q_i + E_{ts,i}}{-2\pi V_{ts,i}}, \tag{20}$$

where, $i = 1, 2$ and A_i^{ratio} is the amplitude ratio for the i^{th} mode A_i / A_{0i}.

The tip-sample interaction force (F_{ts}) in Eqn. (18) can, in principle, be calculated using any appropriate contact model. Here, the AFM tip-surface interactions on viscoelastic polymers are computed using the accelerated Attard's model with a SLS constitutive model for viscoelasticity, except otherwise specified. The creep compliance function of the SLS constitutive model is:

$$\frac{1}{E(t)} = \frac{1}{E_\infty} + \frac{E_\infty - E_0}{E_0 E_\infty} e^{-t/\tau}, \tag{21}$$

that includes a single relaxation time, which governs how fast the instantaneous modulus of the sample changes from E_0 (short-term modulus of the sample) to E_∞ (long-term modulus once the material is completely relaxed). Attard's three-dimensional viscoelasticity model correlates the radial time-dependent sample surface deformation, $u(r,t)$, to its rate of change, $\dot{u}(r,t)$, through its interaction with an axisymmetric rigid tip[21]:

$$\dot{u}(r,t) = -\frac{1}{\tau}\left(u(r,t) - u_\infty(r,t)\right) - \frac{1}{E_0}\int_0^\infty k(r,s)\, \dot{p}(h(s,t))\, s\, ds, \tag{22}$$

where $p(h(r,t))$ is the interaction force per unit area (pressure) between the tip and the surface. $p(h(r,t))$ is a function of $h(r,t)$ which is the radial time-dependent gap between the axisymmetric tip and the deformed sample at time t and radius r from the central axis. In this work, we calculate $p(h(r,t))$ based on the Lennard-Jones pressure equation:

$$p(h(r,t)) = H / 6\pi h(r,t)^3 \left(z_0^6 / h(r,t)^6 - 1\right), \tag{23}$$

where z_0 and H are the intermolecular equilibrium distance and Hamaker constant, respectively. Also, $\dot{u}(r,t)$ and $\dot{p}(h(r,t))$ are time derivatives of $u(r,t)$ and $p(h(r,t))$, respectively. The long-time deformation of the surface, $u_\infty(r,t)$, is defined as:

$$u_\infty(r,t) = -\frac{1}{E_\infty}\int_0^\infty k(r,s)\, p(h(s,t))\, s\, ds, \tag{24}$$

and the kernel of the integral, $k(r,s)$, can be expressed in terms of the complete elliptic integral of the first kind[40], K, as shown below:

$$k(r,s)=\begin{cases}\frac{4}{\pi r}K(s^2/r^2) & s<r\\ \frac{4}{\pi s}K(r^2/s^2) & s>r\end{cases}. \qquad (25)$$

Attard's model parameters and the associated computational methods are elaborated elsewhere[20].

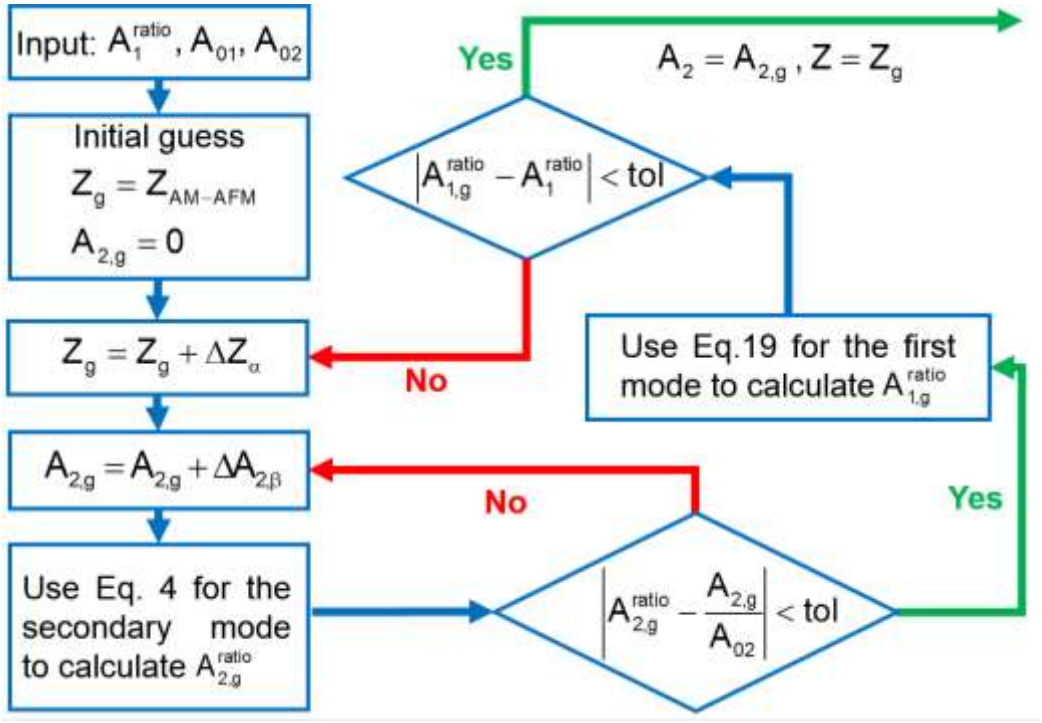

Figure 2. The algorithm proposed in this work for predicting instrument observables in bimodal AFM through simultaneous compliance of the amplitude reduction formulas for both driven modes. Subscripts 1 and 2 for the parameters denote the first and secondary excited modes. The secondary mode is often the second eigenmode of the microcantilever, but it can instead be any higher-order eigenmode. The subscript "g" denotes a guessed value for a parameter and the subscripts "α" and "β" represent the number of iterations of each loop of the algorithm.

To embed Attard's model into the bimodal AFM framework, we propose an algorithm (Figure 2) that can predict the Z distance and associated ϕ_1, A_2, and ϕ_2 for a given A_1^{ratio}

, A_{01}, and A_{02}. In this algorithm, we assume the cantilever is simultaneously excited exactly at two of its eigenfrequencies (i=1 and i=2) and the relevant parameters are labeled accordingly. The algorithm simultaneously satisfies the amplitude reduction formulas (Eqn. (19)) for both excited modes and computes the resulting bimodal phases (Eqn. (20)). $Z_g = Z_{AM-AFM}$ is the initially guessed Z value using a previously proposed algorithm for AM-AFM[20]. ΔZ_α and $\Delta A_{i,\beta}$ are the adjustments made to Z and A_i at each iteration, respectively which are applied to the guessed values to facilitate the convergence process. These values (ΔZ_α and $\Delta A_{i,\beta}$) are updated at each iteration to achieve accelerated convergence. When both loops are satisfied as directed by the algorithm, all bimodal AFM parameters such as Z, indentation, second mode amplitude, energy dissipations, and virials are recorded for the given set of input parameters. A tolerance ("tol" as shown in Figure 2) of 10^{-2} which facilitates a reasonable accuracy is used to fulfill the condition of the algorithm.

3. Verification of the amplitude reduction algorithm

To verify Eqn. (19) and (20), the predictions from the proposed algorithm are compared to experimental data from literature[13] extracted on a stiff (silicon) elastic sample and simulation results from the AMAC (amplitude modulated approach curves) tool of VEDA (Virtual Environment for Dynamic AFM) which includes explicit microcantilever dynamics in bimodal AFM[41]. The interaction force (F_{ts}) is calculated using the DMT (Derjaguin, Muller, and Toporov) model[42], and the surface and interaction parameters[13] are mentioned in the caption of Figure 3. The results from the algorithm show an excellent agreement with the experimental and simulation data. In these simulations, the tip oscillates in the attractive regime ($\phi_1 > 90^\circ$).

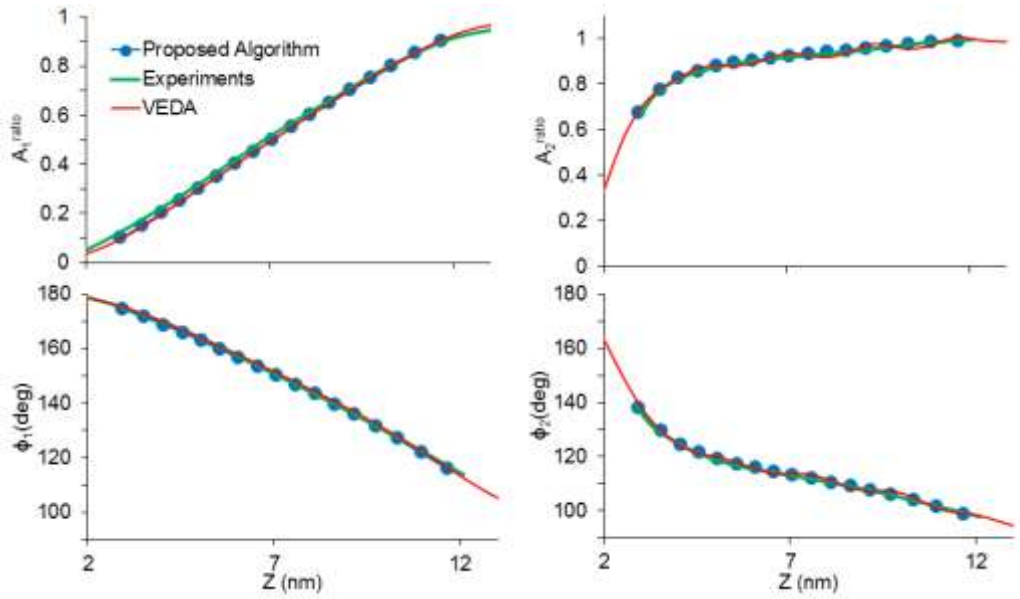

Figure 3. Validation of Eqn.'s (19) and (20) against previously published bimodal AFM experimental data [13] and simulation results extracted using the AMAC tool of VEDA [41] on a Silicon sample illustrates excellent agreement. The A_1^{ratio} range used for these simulations is between 0.1 and 0.9. The employed parameters in these simulations are as follows: $A_{01} = 10\,\text{nm}$, $A_{02} = 1\text{nm}$, $H = 9.03\times10^{-20}\,\text{J}$, $k_1 = 0.9\,\text{N/m}$, $k_2 = 35.2\,\text{N/m}$, $f_1 = 48.913\,\text{kHz}$, $f_2 = 306.194\,\text{kHz}$, $Q_1 = 255$, and $Q_2 = 1000$ [13].

To examine the accuracy of the model predictions when the tip-surface interaction is in the repulsive regime, we conducted another set of simulations on a softer elastic surface whose parameters are mentioned in the caption of Figure 4. The interaction force (F_{ts}) is calculated using the DMT model. The predictions from the proposed algorithm (Figure 4) again show excellent consistency with the results of VEDA tools for this scenario in which the oscillation regime is repulsive ($\phi_1 < 90^\circ$) (Figure 4).

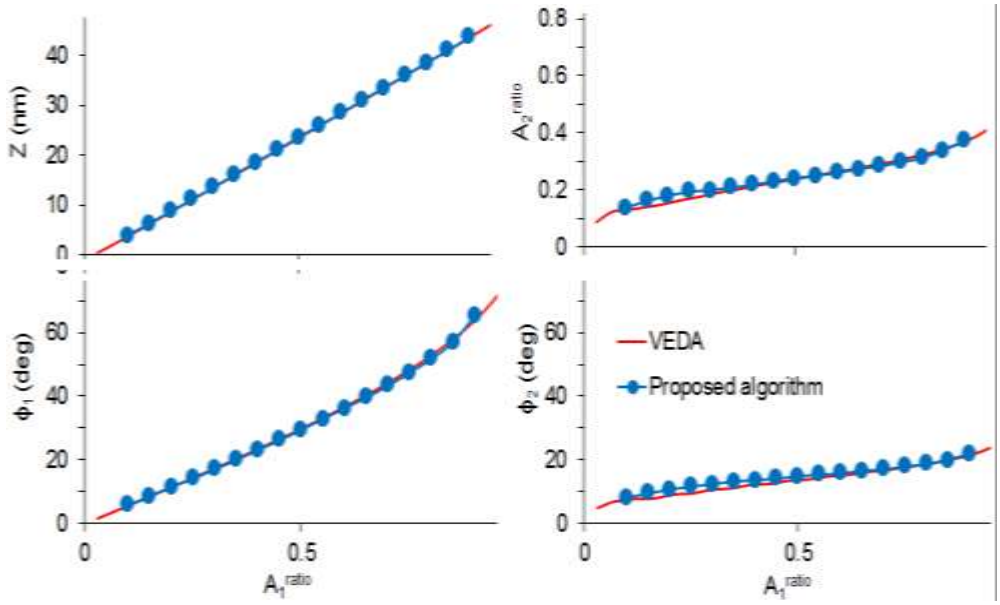

Figure 4. Validation against bimodal AFM simulation results extracted using the AMAC tool of VEDA [41] on an elastic sample illustrates perfect agreement with the proposed algorithm. The used values for material properties, microcantilever, and DMT model parameters are: $A_{01} = 50\,\text{nm}$, $A_{02} = 1\text{nm}$, $f_2/f_1 = 6.26$, $E = 1\,\text{GPa}$, and $H = 7.55\times10^{-20}\,\text{J}$. The Ar_1 range used for these simulations is between 0.1 and 0.9.

4. Computational results

To predict the dependence of bimodal AFM observables on adhesive and viscoelastic properties of local polymeric domains using the proposed Attard's model, we conduct a set of simulations using typical viscoelastic polymer properties[43]. The values for operational parameters and the cantilever properties are chosen in range with what is commonly used for bimodal AFM experiments on polymers. In this set of simulations, different creep (retardation) times (τ) ranging between 3.2×10^{-5} s and 3.2×10^{-10} s are employed in the simulations while all other parameters are held fixed. This range for τ was chosen to span timescales ranging from much smaller to much larger than tip-surface interaction time. Olympus AC160-R3 microcantilever property values calibrated experimentally are used in these simulations: $f_1 = 280\,\text{kHz}$, $k_1 = 28.1\text{N/m}$, $Q_1 = 430$, $f_2 = 1593\,\text{kHz}$, and $Q_2 = 600$. The calibration methods are explained in the experimental section. A_{01} and A_{02} are selected to be $50\,\text{nm}$ and 1nm, respectively. We specifically

chose a small A_{02}/A_{01} ratio to avoid crosstalk between modes as suggested by others [33, 36, 44, 45]. The surface properties used are listed in Table 2.

Table 2. The surface properties that are used to predict the dependence of bimodal AFM observables on local adhesive and viscoelastic polymer properties using the proposed algorithm.

τ	E_0	E_∞	H	z_0	ν
varies	2.0 GPa	0.5 GPa	5×10^{-20} J	0.28 nm	0.49

Simulation results for observables, $V_{ts,i}$, and $E_{ts,i}$ $(i=1,2)$ of bimodal AFM are illustrated in Figure 5 as a function of A_1^{ratio} (solid lines, horizontal axis at the bottom) and τ (dotted lines, horizontal axis on the top). As discussed elsewhere [20], the calculated values for ϕ_1 (Figure 5-a), which depend on the average dissipated energy during each interaction cycle[46], are a function of the ratio between the interaction time (the duration on which the tip experiences surface forces) and the effective relaxation (or creep) time for viscoelastic samples. When $\tau \ll$ contact time or $\tau \gg$ contact time, the polymer is either nearly completely relaxed or relaxes very little during the interaction time, respectively. In both these cases, minimal hysteresis occurs during tapping cycles. However, when τ value gradually changes between these two extremes, energy dissipation during each interaction cycle appears, rises to its maximum, and then gradually vanishes. This phenomenon leads to the non-monotonic behavior of ϕ_1 and $E_{ts,1}$ vs. τ for a fixed A_1^{ratio} in Figure 5 (a and e) as observed previously for tapping mode[20] on viscoelastic and adhesive surfaces.

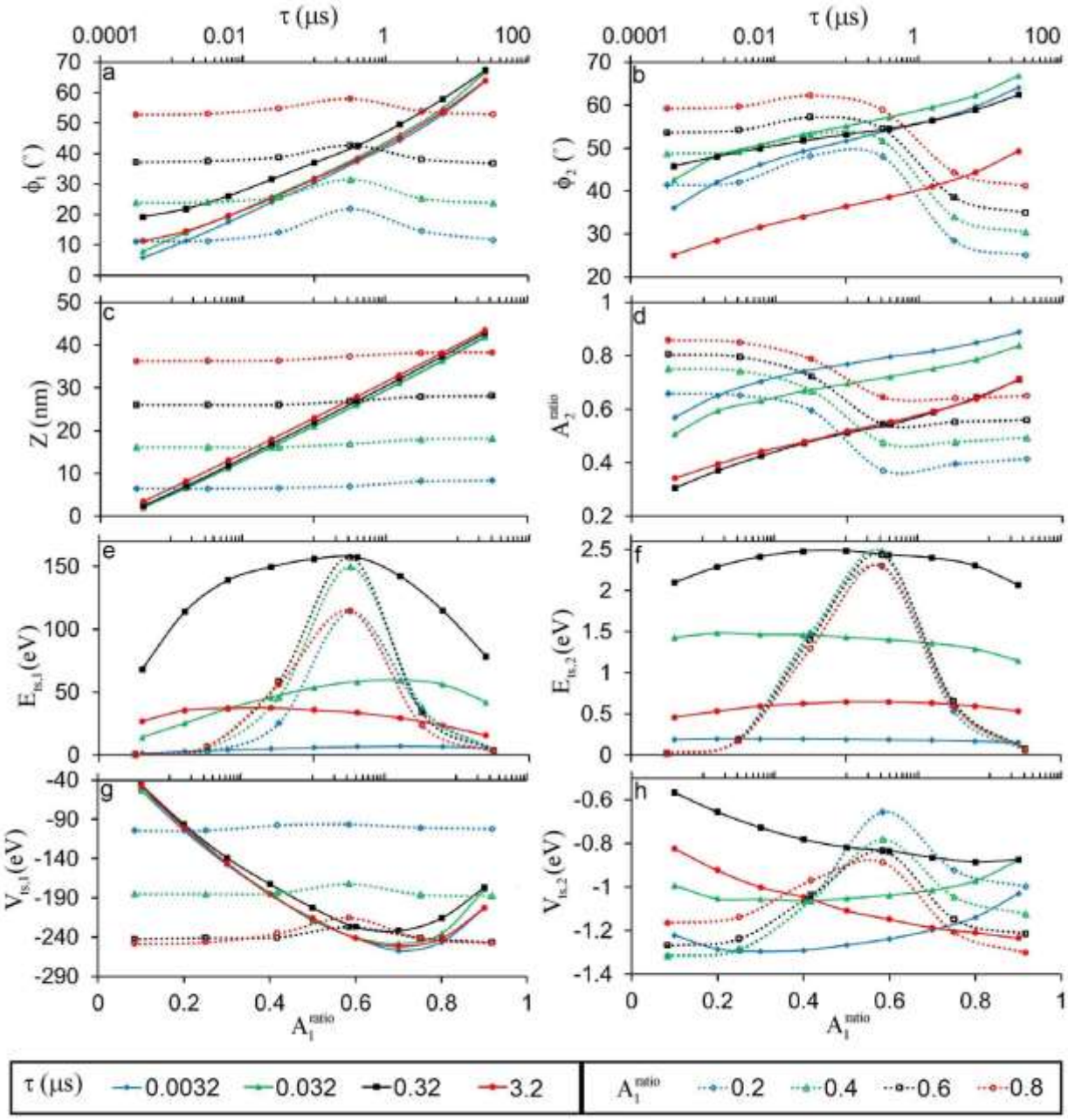

Figure 5. Study of the bimodal AFM observables' sensitivity to the effective creep time of the polymer (τ) and amplitude ratio of the first mode (A_1^{ratio}). The prediction values connected with dotted and solid lines share the same A_1^{ratio} and τ, respectively, as specified in the legend. The range of selected τ values is between 32 μs to 3.2×10^{-4} μs and the selected A_1^{ratio} values are between 0.1 to 0.9. The horizontal axis for the dotted and solid lines are located at the top (log scale) and bottom of the graphs, respectively.

Figure 5 provides key insights into the sensitivity of bimodal AFM observables to local changes in τ while scanning a hypothetical sample where other parameters such as E_∞ and E_0 are held constant. While ϕ_1 changes more sensitively with A_1^{ratio} than ϕ_2, when the main difference between two adjacent domains on the surface is their associated effective relaxation time, ϕ_2 can discriminate much more effectively between regions where τ is much smaller or much larger than the contact time. A clue to the underlying reasons for this behavior can be found in Figure 5 f and h which show that across the five orders of magnitude changes in τ studied, the range of computed values for $V_{ts,2}$ is much smaller than the range of ones attained for $E_{ts,2}$. When combined with the fact that $\pi k_2 A_2^{\,2}/Q_2 \ll \pi k_1 A_1^{\,2}/Q_1$ due to the amplitude difference between modes, the resulting ϕ_2 (Eqn. (20)) thus depends proportionally more on $E_{ts,2}$ and $V_{ts,2}$ compared to the dependence of ϕ_1 on $E_{ts,1}$ and $V_{ts,1}$. For these reasons ϕ_2 appears more sensitive than ϕ_1 to changes in τ. In addition, the amplitude of the second mode (A_2), as depicted in Figure 5 (b), monotonically changes with relaxation time. As illustrated, for the same first mode amplitude setpoint, when $\tau \ll$ contact time and the sample's elastic modulus is ~ E_∞ (softer), A_2 is larger than when $\tau \gg$ contact time and the sample's elastic modulus is ~ E_0 (stiffer). In both of these cases, since the energy dissipation due to viscoelasticity is ≈ 0, according to Eqn. (18), A_2 is correlated to ϕ_2 as follows: $A_2 = A_{02}\sin(\phi_2)$ and therefore, ϕ_2 and A_2 are directly related.

When $(A_{02}/\text{indentation depth} << 1)$, the interaction time in bimodal AFM is mainly dictated by the first mode frequency and is not substantially influenced by the secondary mode frequency. Therefore, as long as $(A_{02}/\text{indentation depth} << 1)$, our previous studies on the relaxation mode(s) of a polymer sample that contributes the most to energy dissipation during a tapping cycle of AM-AFM [20] is indeed applicable to bimodal AFM. Thus, the relaxation behavior of the sample when examined by such configuration of bimodal AFM can be represented by constitutive models with one single effective relaxation time, like SLS, Kelvin-Voigt, or Maxwell models. However, the Kelvin-Voigt

model exhibits no stress relaxation when the surface is under a constant strain and the Maxwell model does not lead to surface restoration to its original state after the applied stress is removed. Hence, hereinafter we select to use the SLS model with a fixed relaxation time to model the viscoelastic response of the evaluated polymeric samples in this article. The assessed samples' viscoelastic behavior is properly represented by selecting adjusted E_0 and E_∞ values. Particularly about tapping mode AFM, microcantilever's fundamental mode resonances are usually of the order of magnitude of 100's of kHz with tip oscillation time periods of the order of 10's of microseconds. As we have described in prior work[20], in gentle tapping conditions the tip-sample interaction time often is of the order of magnitude of 1/10th of the tip oscillation period, or of the order of microseconds. Our prior work[20], also shows that the relaxation mode that has the most effect on AFM observables is in the range of /10th of the tip-sample interaction time, or of the order of 0.1 microseconds. Furthermore, our prior work[20] also describes that the AFM observables change significantly only when the relaxation time used changes by several orders of magnitude. This justifies the use of 0.1 microseconds as the correct order of magnitude of the substrate relaxation time that most affects the AFM observables and will be used henceforth in this article.A comprehensive study of the dependence of bimodal AFM observables on local adhesive and viscoelasticity parameters for a fixed τ is presented in Figure 6. The microcantilever properties, A_{01}, and A_{02} of these simulations are identical to the ones used for Figure 5 and the A_1^{ratio} is 0.5. The simulation results for various viscoelasticity model parameters and two different surface adhesions are presented in Figure 6. The identical parameters used for these simulations are: $R = 3\,\text{nm}$, $A_1^{ratio} = 0.5$, and $\tau = 0.1\,\mu\text{s}$. The Poisson ratio (ν) for the LDPE and PS domains are chosen as the nominal values provided by the manufacturer, 0.49 and 0.35, respectively. E_0 and E_∞ values for the simulations are selected based on the Latin hypercube sampling method.

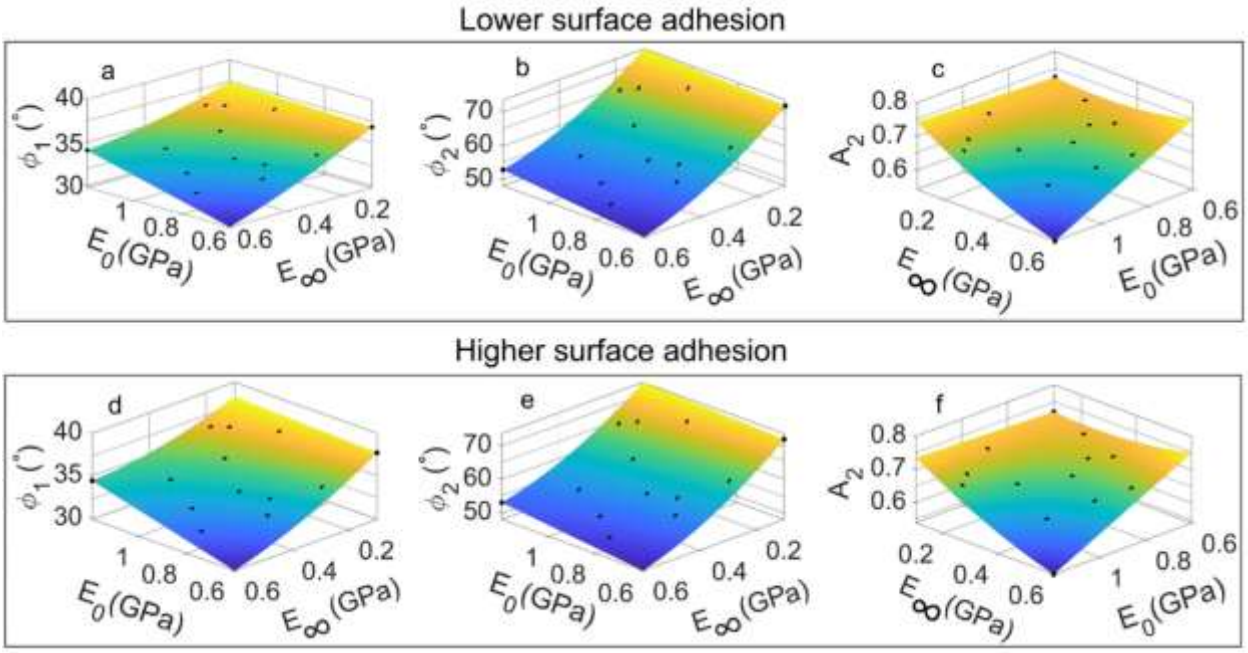

Figure 6. Study of the bimodal AFM observables' dependence on the surface adhesion (quantified as $HR/6z_0^2$) and viscoelasticity level. The first row (a-c) and second row (d-f) simulations have smaller and larger adhesions associated with $H = 1\times10^{-20}$ J and $H = 7\times10^{-20}$ J, respectively. The selection of E_0 and E_∞ in the performed simulations are done based on the "Latin hypercube sampling" method. The used material and interaction parameters are stated in the text. In these conducted simulations $R = 3$ nm, $A_1^{ratio} = 0.5$, $\nu = 0.49$, and $\tau = 0.1\,\mu$s

As seen in Figure 6, the hysteresis due to surface adhesive forces is larger when E_∞ and/or adhesive forces are relatively smaller and larger, respectively. Furthermore, while ϕ_2 is generally more sensitive to changes in surface viscoelasticity, the surface adhesion is better resolved via ϕ_1. The higher sensitivity to the magnitude of surface adhesion of ϕ_1 in comparison with ϕ_2 can be explained through the tip velocity-dependency of the energy dissipation as expressed in Eqn. (18). Therefore, since the adhesive forces between tip and surface during the interaction time occur when the tip experiences the largest first mode velocities, their contribution toward first-mode dissipation weighs more than equally-in-size repulsive forces. This relation holds either during approach or retraction off the surface. However, in terms of the secondary mode energy dissipation contributions, there is no such relation between the tip secondary mode velocity and the adhesive forces.

5. Material viscoelasticity and adhesive properties estimation

We next explore utilizing the proposed computational approach to post-process the experimental observables and estimate the surface adhesive and viscoelastic properties. Since the accelerated Attard model does not provide a closed-form solution, finding a correlation between the experimental data and the surface properties is challenging. Here we present a data analytics approach to connect the bimodal AFM observables to the material's properties through an inverse model.

The data analytics approach requires a comprehensive set of simulations with an appropriate range for E_0, E_∞, surface static adhesion, and tip radius (R) values for known AFM microcantilever properties and operating conditions (k_1, k_2, Q_1, Q_2, A_{01}, A_1^{ratio}, A_2^{ratio}). Assuming the employed cantilever's fundamental frequency is in the order of 100's of kHz, we select $\tau = 10\mu s$ for the SLS model with the same reasoning described in the previous section. The inclusive bimodal AFM observables database with known input parameters facilitates a regression-based analysis to identify and recognize the existing dataset patterns. We used a method based on the multivariate linear regressions to estimate E_0, E_∞, and surface static adhesion from the measured ϕ_1, ϕ_2, and A_2 values at each pixel. To minimize the precision loss due to using linear regression, the range of E_∞ used for generating the simulation results dataset is selected in accordance with the reported quasi-static material stiffness. The R process utilized can be represented as a conversion matrix and vector, as follows:

$$\begin{Bmatrix} \phi_1 \\ \phi_2 \\ A_2 \end{Bmatrix} = \begin{bmatrix} c_1 & c_2 & c_3 \\ c_4 & c_5 & c_6 \\ c_7 & c_8 & c_9 \end{bmatrix} \begin{Bmatrix} E_0 \\ E_\infty \\ Adh \end{Bmatrix} + \begin{Bmatrix} d_1 \\ d_2 \\ d_3 \end{Bmatrix} \quad (26)$$

To better describe the utilized mapping process, the calculated c_i and d_i constants for PS and LDPE polymer samples are listed in Table 3. Due to the large stiffness difference between PS and LDPE, using a single simulation results dataset that covers this large stiffness range is a time-consuming process. Furthermore, using linear regression to figure out the constant terms of the conversion matrix/vector over a large range for

stiffness parameters may not lead to a proper approximation accuracy. Therefore, we prepared two dedicated sets of simulation result datasets for PS and LDPE in which, the selected ranges for E_∞ values are 1-3 GPa and 0.2-0.6 GPa, respectively. These ranges are chosen based on the reported quasi-static stiffness of these materials over which conducting stable simulations is achievable. The E_0 range for each of these datasets is selected accordingly. The Poisson ratio (ν) for the LDPE and PS are chosen as the nominal values provided by the manufacturer, 0.49 and 0.35, respectively.

Table 3. The coefficients of the conversion matrix and vector as described in Eqn. (26) determined through linear regression on simulation results. The tip radius estimate is 8.7 nm.

	c_1 (GPa)	c_2 (GPa)	c_3 (GPa/nm)	c_4 (GPa)	c_5 (GPa)	c_6 (GPa/nm)
PS	0.89	6.81	-0.21	0.14	-33.72	0.15
LDPE	0.23	2.41	-0.07	0.07	-1.24	-0.003
	c_7 (nN)	c_8 (nN)	c_9 (Pa)	d_1 (GPa)	d_2 (GPa)	d_3 (nN)
PS	0.18	-1.62	-0.14	-22.54	8.36	-0.08
LDPE	0.008	0.69	-0.02	-4.06	-0.49	0.99

6. Experiments

To validate the performance of the described inverse approach, we acquired a set of experimental bimodal AFM data on a polymer blend sample and used it to estimate its viscoelastic and adhesive properties. The bimodal AFM experiments are performed using a commercial Cypher AFM setup (Asylum Research, Santa Barbara, CA) on a fresh PS-LDPE polymer blend which was purchased from Bruker Nano Inc. The experiments are performed on a $4\times4\ \mu m$ rectangular region with a 1024 points/line resolution level and a scan rate of 1 Hz. The sample is selected due to the significant mechanical difference between polymer domains, as the bulk nominal Young's modulus for PS and LDPE are 2 GPa and 0.1 GPa, respectively, as per the product description. By calibrating Olympus AC160 microcantilevers, the following parameters are determined: $f_1 = 281 kHz$, $f_2 = 1.593\,MHz$, $k_1 = 28.1 Nm^{-1}$, $k_2 = 509.8\,Nm^{-1}$, $Q_1 = 429$, $Q_2 = 600$, $A_{01} = 50\,nm$, and

$A_{02} = 1\text{nm}$. The calibration of the first mode stiffness was performed based on two well-established calibration techniques: the Sader method [47] and the thermal noise method[48]. This arrangement which does not require mechanical contact with a hard sample during the calibration is accessible through the GetReal™ tool in the instrument software. The calibration of the second mode stiffness was performed using the suggested power-law relationship between stiffness and frequencies of the excited modes: $k_2 = k_1\left(f_2/f_1\right)^{\xi_2}$, where ξ_2 is the calibration parameter which is empirically determined for specific microcantilevers[49, 50]. The calibration values obtained using the mentioned method were compared with the ones from the slope of the dynamic amplitude approach curve for the second eigenfrequency and the one for the quasi-static force curve for the first resonance mode on a fresh clean silicon sample and the agreement of the acquired values was satisfactory. The blueDrive photothermal excitation system excites the microcantilever at two eigenfrequencies (1 and 2). Modal amplitudes and phases were tuned when the microcantilever was within 100 nm above the surface. We specifically suggest A_1^{ratio} at 0.5 for the experiments to maximize the energy dissipation during each cycle[20]. The experiments were conducted under ambient temperature and dry nitrogen flushed conditions to minimize the effect of capillary forces. As shown in Figure 7, The polymeric domains are well separated. The round shapes on the images are LDPE domains which are surrounded by a homogeneous PS background. We use the bimodal observables of each pixel of the images, i.e. ϕ_1, ϕ_2, and A_2, to estimate the surface nanoscale properties using the regression model (Eqn. (24)).

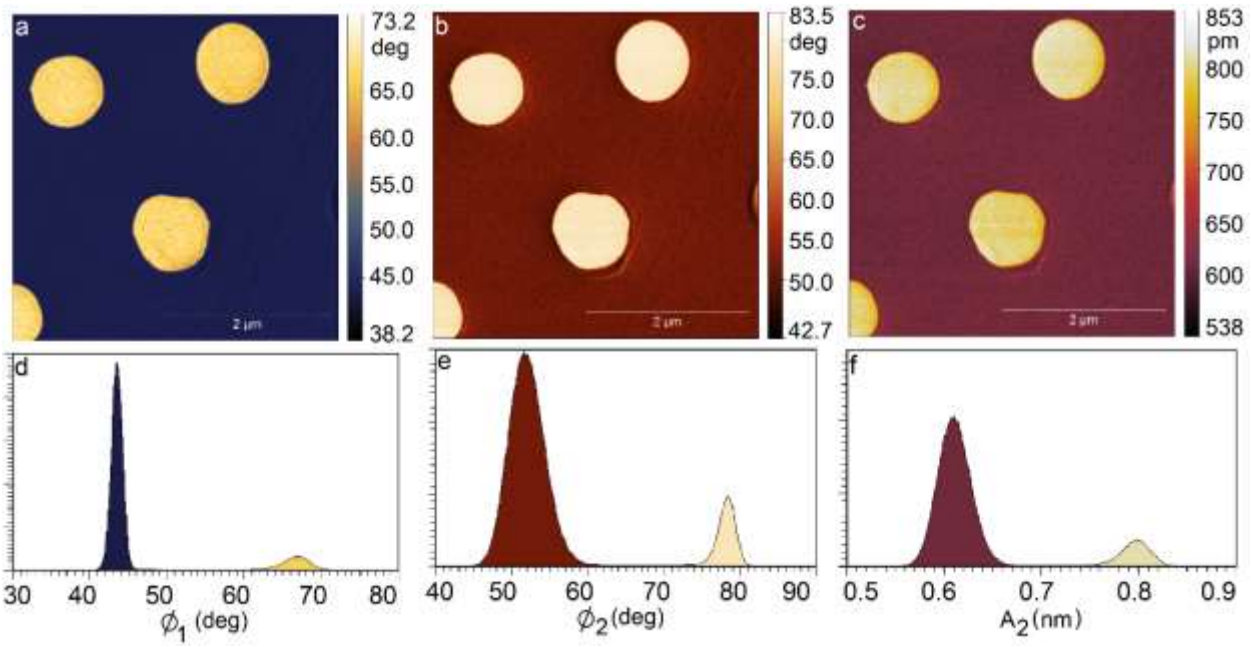

Figure 7. Bimodal AFM images of the PS-LDPE sample illustrate phase lag of the first and second mode, and amplitude of the 2nd mode from left to right, respectively. The associated histograms are shown in the second row. The size of the images is 4×4 μm .

The spatially resolved surface properties estimations using the described inverse approach are shown in Figure 8 and the predicted mean values for polymer domains are listed in Table 4. Since similar samples were previously explored by others, here we compare our results with their predictions. Garcia et al.[14] presented a method in which the model parameters were first calibrated on the PS domain so that the model prediction for PS stiffness becomes comparable with expected values. Then, the calibrated model was applied to LDPE domain leading to stiffness estimates of 0.11 ± 0.02 GPa which compares well to our E_∞ value prediction as listed in Table 4. In their method, the viscoelasticity of the surface was described by a so-called "3D Kelvin–Voigt model" in which the surface adhesion is neglected. Meng et al.[51] employed DMT model to estimate the PS-LDPE surface adhesion and stiffness using magnetic-drive soft probes. The resultant mean reduced modulus predictions for PS and LDPE phases were 0.1 and 1.8 GPa, respectively which compare well to our results. Since each group used different microcantilevers to conduct experiments, we compare the predicted adhesion force values for PS and LDPE phases through the ratio of the mean predicted adhesions for

these domains. Meng et al.[51] and Solgaard et al.[26] reported adhesions ratios as 1.26 and 1.2~2.0, respectively, which is in agreement with 1.29 predicted by our method. Therefore, the results demonstrate the capability of the inverse model based on Attard's approach to make realistic predictions on the sample's viscoelastic and adhesive properties based on the acquired bimodal AFM observables (i.e. ϕ_1, A_2, and ϕ_2).

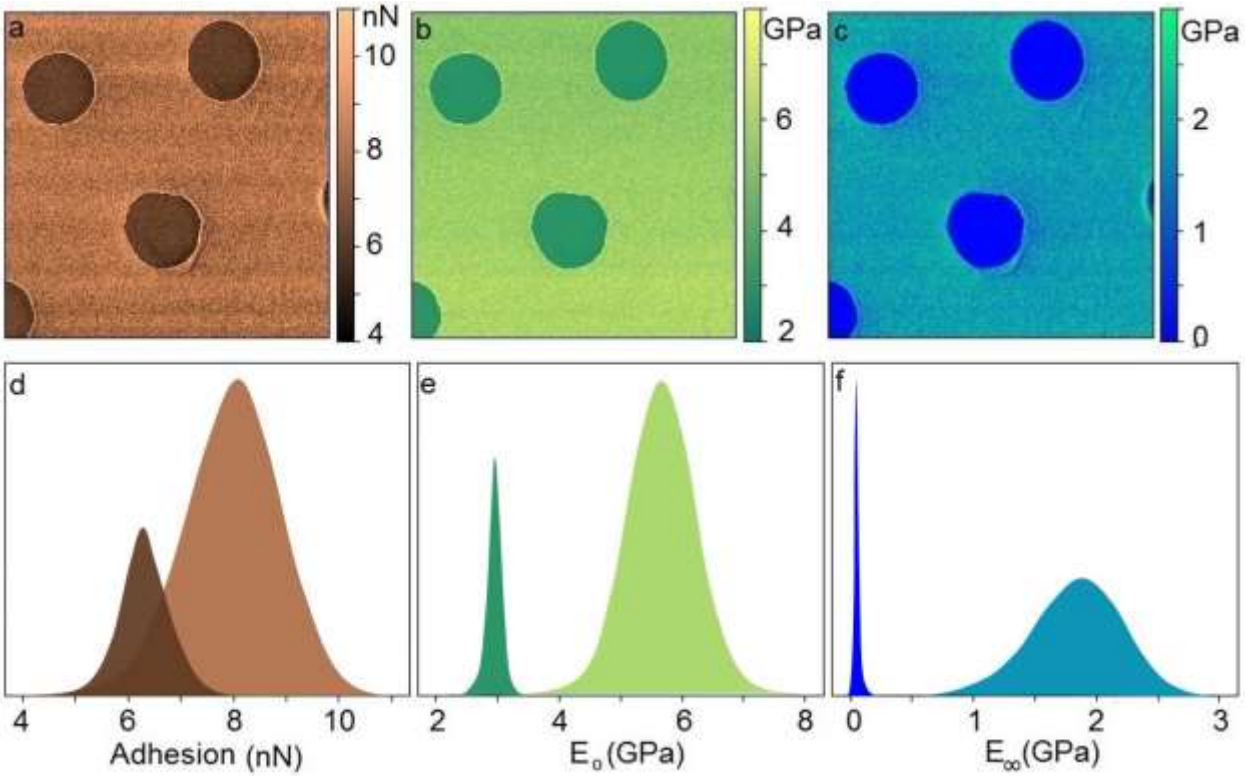

Figure 8. The estimates for adhesion force, E_∞ and E_0 values for the scanned polymer domains are predicted using the proposed algorithm. The static adhesion is calculated based on $HR/6z_0^2$.

Table 4. Predicted mean viscoelastic properties for the polymer domains based on the acquired bimodal AFM data. The predictions are in agreement with the ones in the literature [14, 26, 51].

domain	E_0(GPa)	E_∞(GPa)	Static Adhesion (nN)
PS	5.68 ± 0.31	1.82 ± 0.31	8.08 ± 0.91
LDPE	2.73 ± 0.11	0.11 ± 0.03	6.28 ± 0.22

7. Conclusions

This work features a proposed algorithm that systematically accommodates surface forces and linear viscoelastic three-dimensional deformation into the bimodal AFM framework. To establish the algorithm, we derived the amplitude reduction formulas for the resonant modes in bimodal AFM based on the Euler Bernoulli assumption for the microcantilever behavior. The algorithm simultaneously satisfies the derived amplitude reduction formulas for both resonant eigenmodes while the tip-surface interaction is computed using the accelerated Attard's model. The algorithm enables the rigorous prediction and interpretation of bimodal AFM observables with a first-principles approach. Simulations illustrate that bimodal AFM can provide enhanced contrast between domains with relaxation time discrepancies in comparison with the conventional tapping mode AFM. The results show that ϕ_2 channel is more responsive to the viscoelasticity level of the sample than ϕ_1. However, ϕ_1 channel is more sensitive to the surface adhesion level than ϕ_2. Furthermore, simulations showed that the phase lag and amplitude ratio of the secondary mode illustrates a nonmonotonic and monotonic variation versus relaxation time, respectively. Then, we presented an inverse regression-based method that quantitatively predicts the local adhesion and standard linear solid viscoelastic parameters from acquired bimodal AFM data. The application of this method on bimodal AFM data on a PS-LDPE polymer blend leads to quantitative discrimination of adhesion and viscoelastic properties of the sample. Taken together, the results presented here successfully open the way to advanced interaction models to be used to quantify local nanomechanical properties of soft, adhesive, and viscoelastic materials in bimodal AFM. However, there is still room for improvement on the model's performance, e.g. the method requires computationally expensive post-processing due to the non-existence of a close-form solution for the utilized contact model, and pre-knowledge about a sample is required to set the right range of E_0 and E_∞.

References

1. R. Garcia and E. T. Herruzo, Nature nanotechnology, 2012, **7**, 217.
2. R. García, R. Magerle and R. Perez, Nature Materials, 2007, **6**, 405.
3. T. R. Rodrıguez and R. García, Applied Physics Letters, 2004, **84**, 449-451.
4. D. Forchheimer, R. Forchheimer and D. B. Haviland, Nature communications, 2015, **6**, 6270.
5. R. W. Stark, N. Naujoks and A. Stemmer, Nanotechnology, 2007, **18**, 065502.
6. O. Sahin, S. Magonov, C. Su, C. F. Quate and O. Solgaard, Nature Nanotechnology, 2007, **2**, 507.
7. E. T. Herruzo, A. P. Perrino and R. Garcia, Nature communications, 2014, **5**, 3126.
8. E. T. Herruzo, H. Asakawa, T. Fukuma and R. Garcia, Nanoscale, 2013, **5**, 2678-2685.
9. S. Santos, C.-Y. Lai, T. Olukan and M. Chiesa, Nanoscale, 2017, **9**, 5038-5043.
10. A. Labuda, M. Kocuń, W. Meinhold, D. Walters and R. Proksch, Beilstein journal of nanotechnology, 2016, **7**, 970.
11. X. Xu, J. Melcher, S. Basak, R. Reifenberger and A. Raman, Physical review letters, 2009, **102**, 060801.
12. R. Proksch, Applied Physics Letters, 2006, **89**, 113121.
13. J. R. Lozano and R. Garcia, Physical Review Letters, 2008, **100**, 076102.
14. S. Benaglia, C. A. Amo and R. Garcia, Nanoscale, 2019, **11**, 15289-15297.
15. R. Garcia and R. Proksch, European Polymer Journal, 2013, **49**, 1897-1906.
16. M. Kocun, A. Labuda, W. Meinhold, I. Revenko and R. Proksch, ACS Nano, 2017, **11**, 10097-10105.
17. W. C. Oliver and G. M. Pharr, Journal of materials research, 1992, **7**, 1564-1583.
18. J. Melcher, C. Carrasco, X. Xu, J. L. Carrascosa, J. Gómez-Herrero, P. J. de Pablo and A. Raman, Proceedings of the National Academy of Sciences, 2009, **106**, 13655-13660.
19. M. Chyasnavichyus, S. L. Young and V. V. Tsukruk, Japanese Journal of Applied Physics, 2015, **54**, 08LA02.
20. B. Rajabifar, J. M. Jadhav, D. Kiracofe, G. F. Meyers and A. Raman, Macromolecules, 2018, **51**, 9649-9661.
21. P. Attard, Langmuir, 2001, **17**, 4322-4328.
22. P. Attard, Physical Review E, 2001, **63**, 061604.
23. J. Boussinesq, Application des potentiels à l'étude de l'équilibre et du mouvement des solides élastiques: principalement au calcul des déformations et des pressions que produisent, dans ces solides, des efforts quelconques exercés sur une petite partie de leur surface ou de leur intérieur: mémoire suivi de notes étendues sur divers points de physique, mathematique et d'analyse, Gauthier-Villars, 1885.
24. T. Ting, Journal of Applied Mechanics, 1966, **33**, 845-854.
25. M. D. McKay, R. J. Beckman and W. J. Conover, Technometrics, 2000, **42**, 55-61.

26. A. F. Sarioglu, S. Magonov and O. Solgaard, Applied Physics Letters, 2012, **100**, 053109.
27. S. Santos, Applied Physics Letters, 2013, **103**, 231603.
28. J. E. Sader, Journal of Applied Physics, 1998, **84**, 64-76.
29. X. Xu, M. Koslowski and A. Raman, Journal of Applied Physics, 2012, **111**, 054303.
30. J. Melcher, S. Hu and A. Raman, Applied Physics Letters, 2007, **91**, 053101.
31. C. P. Green and J. E. Sader, Journal of applied physics, 2005, **98**, 114913.
32. S. Basak, A. Raman and S. V. Garimella, Journal of applied physics, 2006, **99**, 114906.
33. A. M. Gigler, C. Dietz, M. Baumann, N. F. Martinez, R. García and R. W. Stark, Beilstein journal of nanotechnology, 2012, **3**, 456.
34. S. Basak and A. Raman, Applied Physics Letters, 2007, **91**, 064107.
35. T. R. Rodrıguez and R. García, Applied Physics Letters, 2002, **80**, 1646-1648.
36. R. W. Stark, Applied Physics Letters, 2009, **94**, 063109.
37. B. Anczykowski, B. Gotsmann, H. Fuchs, J. Cleveland and V. Elings, Applied Surface Science, 1999, **140**, 376-382.
38. O. Sahin, C. F. Quate, O. Solgaard and A. Atalar, Physical Review B, 2004, **69**, 165416.
39. C.-Y. Lai, V. Barcons, S. Santos and M. Chiesa, Journal of Applied Physics, 2015, **118**, 044905.
40. P. Attard and J. L. Parker, Physical Review A, 1992, **46**, 7959.
41. J. Melcher, S. Hu and A. Raman, Review of Scientific Instruments, 2008, **79**, 061301.
42. B. V. Derjaguin, V. M. Muller and Y. P. Toporov, Journal of Colloid and interface science, 1975, **53**, 314-326.
43. H. F. Brinson and L. C. Brinson, Polymer engineering science and viscoelasticity, Springer, 2008.
44. D. Kiracofe, A. Raman and D. Yablon, Beilstein journal of nanotechnology, 2013, **4**, 385.
45. N. Martinez, S. Patil, J. R. Lozano and R. Garcia, Applied Physics Letters, 2006, **89**, 153115.
46. N. F. Martínez and R. García, Nanotechnology, 2006, **17**, S167.
47. J. E. Sader, J. W. M. Chon and P. Mulvaney, Review of Scientific Instruments, 1999, **70**, 3967-3969.
48. J. L. Hutter and J. Bechhoefer, Review of Scientific Instruments, 1993, **64**, 1868-1873.
49. S. Benaglia, V. G. Gisbert, A. P. Perrino, C. A. Amo and R. Garcia, Nature Protocols, 2018, **13**, 2890-2907.
50. A. Labuda, M. Kocun, M. Lysy, T. Walsh, J. Meinhold, T. Proksch, W. Meinhold, C. Anderson and R. Proksch, Review of Scientific Instruments, 2016, **87**, 073705.
51. X. Meng, H. Zhang, J. Song, X. Fan, L. Sun and H. Xie, Nature Communications, 2017, **8**, 1944.